Nano Res. 2011, 4(4): 414–424
DOI 10.1007/s12274-011-0096-y
Research Article

ISSN 1998-0124
CN 11-5974/O4

Block Copolymer-Templated $BiFeO_3$ Nanoarchitectures Composed of Phase-Pure Crystallites Intermingled with a Continuous Mesoporosity: Effective Visible-Light Photocatalysts?

Christian Reitz, Christian Suchomski, Christoph Weidmann, and Torsten Brezesinski (✉)

Institute of Physical Chemistry, Justus-Liebig-University Giessen, Giessen 35392, Germany

Received: 1 November 2010 / Revised: 22 December 2010 / Accepted: 24 December 2010

ABSTRACT

Herein is reported the soft-templating synthesis of visible-light photoactive bismuth ferrite ($BiFeO_3$) nanoarchitectures in the form of thin films using a poly(ethylene-*co*-butylene)-*block*-poly(ethylene oxide) diblock copolymer as the structure-directing agent. We establish that (1) the self-assembled materials employed in this work are highly crystalline after annealing at 550 ˚C in air and that (2) neither the bismuth-poor $Bi_2Fe_4O_9$ phase nor other impurity phases are formed. We further show that there is a distinct restructuring of the high quality cubic pore network of amorphous $BiFeO_3$ during crystallization. This restructuring leads to films with a unique architecture that is composed of anisotropic crystallites intermingled with a continuous mesoporosity. While this article focuses on the characterization of these novel materials by electron microscopy, krypton physisorption, grazing incidence small-angle X-ray scattering, time-of-flight secondary ion mass spectrometry, X-ray photoelectron spectroscopy, UV-vis and Raman spectroscopy, we also examine the photocatalytic properties and show the benefits of the combination of mesoporosity and nanocrystallinity. Templated $BiFeO_3$ thin films (25% porosity) with a direct optical band gap at 2.9 eV exhibit a catalytic activity for the degradation of rhodamine B much better than that of nontemplated samples. We attribute this improvement to the nanoscale porosity, which provides for more available active sites on the photocatalyst.

KEYWORDS

Self-assembly, mesoporous, nanocrystalline, thin films, photocatalysis, multiferroic

1. Introduction

Developments over the past years have clearly shown that multiferroic materials hold great promise for the fabrication of next-generation microelectronics [1, 2]. In particular, advances that have received widespread attention are those that broaden the scope of these materials by utilizing their unique combination of properties. In this context, it is important to note that multiferroics which show coupling between different types of magnetic and ferroelectric order parameters are particularly promising for technological device applications as there is the prospect of controlling the magnetic properties by an external electric field and vice versa [3–5].

Among the few single-phase magnetoelectric multiferroics that have been discovered to date, bismuth ferrite ($BiFeO_3$, BFO) plays an important role

Address correspondence to torsten.brezesinski@phys.chemie.uni-giessen.de

[6, 7]. It is characterized by a rhombohedrally distorted perovskite structure that possesses antiferromagnetic and ferroelectric orders. In recent years, it has been shown that both a large spontaneous polarization and comparatively large magnetoelectric coupling may occur in BFO materials in forms other than bulk [8–10]. Apart from the ferroic order parameters, BFO also has interesting optical characteristics and thus great potential for applications in solid state devices that utilize heterojunction effects and as visible-light photocatalysts [11, 12].

Heterogeneous semiconductor photocatalysis has been the focus of intense research over the past 50 years since this approach offers an alternative means of water purification to commonly used processes, such as chlorination and ozonolysis [13–15]. The number of reports on this subject continues to increase steadily, and it has been pointed out many times that the photocatalytic activity strongly depends on (1) the ability of the catalyst to create electron–hole pairs, (2) recombination rates both in the bulk and at the surface, and (3) on the specific surface area of the photoactive material.

Although the surface area is known to have a profound effect on material properties and performance, the search for novel photocatalysts has been predominantly centered on the control of atomic structure. Perhaps one of the reasons for this is the fact that recombination rates of electron–hole pairs are largely governed by atomic composition and population of structural defect sites.

Even though BFO is a visible-light responsive oxide, bulk forms of this material have not proven to be of much interest for photocatalytic applications because of their insufficient activity. We associate this low activity with both low surface area and the presence of impurity phases. Thus, by creating nanostructured versions of phase-pure BFO we expect to produce effective visible-light photocatalysts whose properties are determined by surfaces and interfaces and not by bulk behavior alone. The synthesis of phase-pure BFO materials, however, is complicated due to the volatility of bismuth and bismuth oxide species and the fact that BFO is metastable with respect to the bismuth-poor $Bi_2Fe_4O_9$ phase between 720 and 1040 K [6, 16].

Surfactant and polymer templating can be used to produce metal oxides with different nanostructures and large surface areas [17–20]. The formation of these materials relies on the solution phase co-assembly of inorganic oligomers with structure-directing agents to produce long-range periodicities reminiscent of lyotropic liquid crystal phases. Amphiphilic block copolymers are particularly attractive as structure-directing agents because of their ability to form a wide variety of superstructures with large repeat distances. Materials in thin film format can be produced by the same template-directed synthesis method but using an evaporation-induced self-assembly (EISA) process [21].

To date, a broad range of nanostructured metal oxides has been made; however, the use of EISA to produce BFO thin films in phase-pure form has not yet been reported. The present work focuses specifically on BFO, a material that we show here can be synthesized with both a mesoporous morphology and nanocrystalline domain structure by utilizing a poly(ethylene-*co*-butylene)-*block*-poly(ethylene oxide) diblock copolymer, referred to as KLE [22, 23], as the structure-directing agent. In addition, we explore the photocatalytic properties of these nanostructured thin film materials and compare the results to samples prepared with no polymer template but under otherwise identical conditions. Through these experiments, the relationships among crystalline domain size, surface area, and photocatalytic activity are examined. Because bulk BFO does not show promising characteristics as a potential visible-light photocatalyst, the present study provides an important opportunity to demonstrate how both mesoporosity and nanocrystallinity can be used to enhance the catalytic properties of a material whose bulk form exhibits rather limited behavior [22, 24].

2. Experimental

2.1 Materials

$Fe(NO_3)_3{\cdot}9H_2O$ (99.9%), $Bi(NO_3)_3{\cdot}5H_2O$ (99.9%), and 2-methoxyethanol (99.8%) were purchased from Sigma–Aldrich. $H[(CH_2CH_2)_{0.67}\{CH_2CH(CH_2CH_3)\}_{0.33}]_{89}(OCH_2CH_2)_{79}OH$ was used as the structure-directing agent.

2.2 Synthesis

A mixture of 116 mg of $Fe(NO_3)_3{\cdot}9H_2O$ and 145 mg of $Bi(NO_3)_3{\cdot}5H_2O$ dissolved in 2 mL of 2-methoxyethanol was combined with 40 mg of KLE. Once the solution was homogeneous, films were produced via spin- or dip-coating on polar substrates. Optimal conditions include 19%–22% relative humidity. For best results, the as-prepared films were heated to 200 °C using a 1 h ramp and aged at this temperature for 2 h. After that, the samples were heated to 550 °C using a 20 min ramp followed by a 10–20 min soak.

2.3 Characterization

Scanning electron microscope (SEM) images were taken with a LEO Gemini 982. Conventional small- and wide-angle X-ray scattering (SAXS and WAXS, respectively) measurements were carried out on an X'Pert PRO diffractometer from PANalytical utilizing a Bragg–Brentano geometry. Grazing incidence SAXS (GISAXS) data were collected at the German synchrotron radiation facility HASYLAB/DESY on beamline BW4 using a MarCCD area detector and a sample–detector distance of 1820 mm. X-ray photoelectron spectroscopy (XPS) spectra were acquired on a Physical Electronics ESCA 5600 spectrometer with a monochromatic Al *Kα* X-ray source (P = 200 W) and multichannel detector OmniIV. The electron takeoff angle to the sample surface was adjusted to 45°. The C 1s signal from adventitious hydrocarbon at 284.6 eV was used as the energy reference to correct for charging. Raman spectra were acquired using the SENTERRA dispersive Raman microscope from Bruker Optics equipped with an objective from Olympus (MPlan N 20x, FN = 22, NA = 0.40) and a Nd:YAG laser (λ = 532 nm, P = 10 mW). The samples were also analyzed by time-of-flight secondary ion mass spectrometry (TOF-SIMS) using a TOF–SIMS 5 from ION-TOF GmbH. A beam of 25 keV Bi^+ focused to a 10 μm spot was used to generate secondary ions. Sputter etching was carried out using a beam of 1 keV Cs^+ (I_0 = 52 nA) focused to a 300 μm spot. Krypton physisorption measurements were performed at 87 K on 80 nm thick BFO films with a total area of 45 cm^2 using the Autosorb-1-MP automated gas adsorption station from Quantachrome Corporation. Optical absorption measurements were carried out on a PerkinElmer Lambda 900 ultra violet-visible-near infrared (UV-vis-NIR) spectrophotometer. A substrate made from fused silica and an aluminum mirror served as the reference for transmission and reflection measurements, respectively. The film thickness was determined with an Alpha Step IQ Surface Profiler from KLA Tencor.

For photodegradation experiments, 8 mL of an aqueous solution of 10 μmol/L rhodamine B was irradiated with 366 nm light (P = 16 W) in the presence of either 75 nm thick KLE-templated or nontemplated films with a total area of 4 cm^2. 366 nm light was chosen for experimental reasons.

3. Results and discussion

The mesoporous BFO thin films employed in this work were prepared by soft-templating using an evaporation-induced self-assembly process. In the synthesis, an isotropic solution made from 2-methoxyethanol, KLE diblock copolymer, and hydrated bismuth and ferric nitrates was dip- or spin-coated onto a polar substrate. On evaporation of 2-methoxyethanol and other volatile constituents, the system co-assembled to form a nanostructured inorganic/organic composite with long-range periodicity. Thermal treatment was then used to further crosslink the inorganic framework, combust the KLE template, and induce the conversion of the amorphous material to nanocrystalline BFO.

As mentioned above, in this work we incorporated a poly(ethylene-*co*-butylene)-*block*-poly(ethylene oxide) diblock copolymer as the structure-directing agent. Unlike the well-known Pluronic-type triblock copolymers, such as P123 and F127, KLE has been shown to be particularly suitable for the direct synthesis of nanocrystalline oxide and non-oxide thin films with ordered cubic networks of 14–18 nm diameter pores and high thermal stability [22, 24, 25]. One reason for this is that KLE produces inorganic/organic composites with 25–30 nm repeat distances, which accommodate walls sufficiently thick to allow for uniform nucleation and growth of the crystalline phase with retention of the periodicity.

To our knowledge, the polymer-directed synthesis of BFO nanoarchitectures in thin film format has not

yet been reported and so the ensuing section will focus on the characterization of these novel materials.

Figure 1 shows both top view and cross-sectional SEM images of a self-assembled BFO thin film before and after removal of the KLE template and crystallization of the inorganic material by heating at 550 ˚C. Figures 1(a) and 1(b) reveal a highly ordered network of pores averaging 18 nm in diameter. It is apparent from both images that the samples are crack-free at the micrometer length scale, and that the presence of major structural defects can be ruled out. In addition, it can be clearly seen that the pores at the hexagonal top surface are open and that the nanoscale structure persists throughout the films (see also Fig. S-1 in the Electronic Supplementary Material (ESM)). From Figs. 1(c) and 1(d), we are able to establish that the film morphology undergoes a change upon conversion of the amorphous inorganic framework. Such changes are particularly evident if larger nuclei are present at the onset of crystallization, which is the case for the BFO materials employed in this work. However, the samples are still crack-free and well-defined at the micrometer level. Also, Figs. 1(c) and 1(d) confirm that the nanoscale porosity is retained throughout the bulk of the films and further show that the crystalline BFO materials are composed of elongated crystallites (see also Fig. S-1 in the ESM). The presence of anisotropic crystallites is not surprising, though, given the structural anisotropy of rhombohedral BFO.

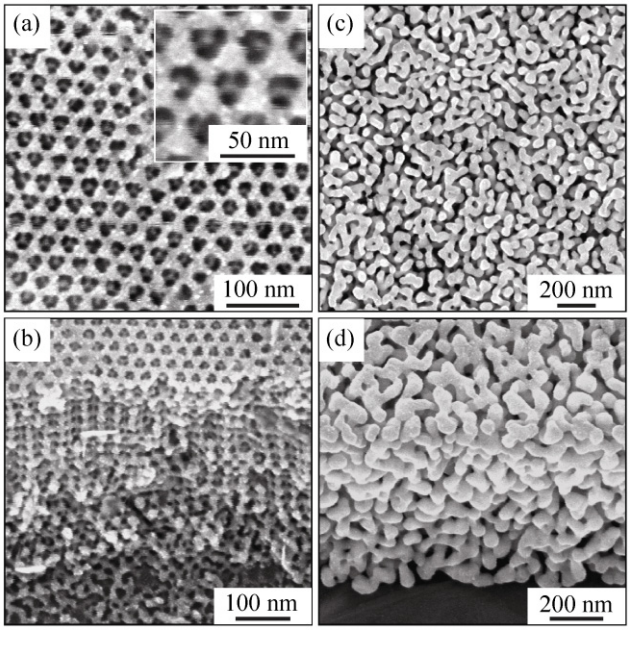

Figure 1 Morphology of KLE-templated BFO thin films calcined at 200 ˚C for 2 h (a, b) and 550 ˚C for 20 min (c, d). (a) SEM image of the ordered hexagonal top surface. A high-magnification image is shown in the inset. (b) Cross-sectional SEM image of a razor blade cut in the same film in (a). (c) Top view SEM image showing that the crystalline BFO material is composed of elongated nanoparticles. (d) Cross-sectional SEM image of the same film in (c)

Overall, electron microscopy demonstrates that calcination at 550 ˚C in air leads to the formation of nanocrystalline thin films with a unique morphology due to restructuring of the high quality pore network of amorphous BFO.

These structure and morphology results are further supported by GISAXS data and conventional SAXS experiments in the Bragg–Brentano geometry. Figure 2 shows GISAXS patterns obtained at an angle of incidence $\beta = 0.2°$ on a KLE-templated BFO thin film before and after crystallization. From this data, it can be seen that amorphous samples produce patterns with distinct maxima. However, these scattering maxima cannot be clearly indexed to a certain cubic phase. KLE-templated materials typically show either a body-centered-cubic (bcc) *Im3m*-derived structure or a face-centered-cubic (fcc) close-packed structure with (111) orientation relative to the substrate [22, 23, 25]. In the case of BFO, by contrast, the scattering maxima can be indexed to both a three-dimensional hexagonal close-packed (hcp) network of pores with (001) orientation and a distorted bcc structure with (110) orientation (see Fig. S-2 in the ESM). At first glance, the hexagonal symmetry of the top surface argues against a bcc phase; however, the orientation at the sample/air interface might be different from that in the bulk of the films. In addition, it is worth mentioning that some smaller domains with square symmetry can be observed by SEM, as shown in Fig. S-1 (in the ESM). Since no conclusions about the orientation can be made on the basis of the data presented in Figs. 1 and 2, we refer to the structure of amorphous BFO thin films as a distorted cubic pore network.

The in-plane d-spacing is approximately 26 nm, which is typical of KLE-templated materials [24, 26]. On the basis of the relative position of the out-of-plane reflections, a lattice contraction of ~70% is determined

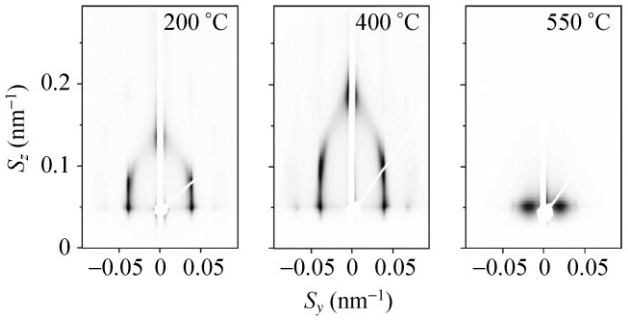

Figure 2 Synchrotron-based GISAXS on a KLE-templated BFO thin film with amorphous and crystalline pore walls. GISAXS patterns were collected at an angle of incidence $\beta = 0.2°$ and show the evolution of the cubic pore network upon thermal treatment. Scattering vector, $\boldsymbol{s}$, components are given in nm^{-1}

normal to the plane of the substrate for films aged at 200 °C for 2 h; the in-plane lattice contraction, by contrast, is negligible as the films are pinned to the substrate. The very same samples reveal a contraction of ~80% after thermal treatment at 250 °C. Higher annealing temperatures (see Fig. S-2 in the ESM), however, do not lead to a further change in volume as the nitrate ligands of both inorganic precursors are fully decomposed by 250 °C. This result is in agreement with previous studies of the thermal decomposition of hydrated bismuth and ferric nitrate [27, 28].

From Fig. 2 it is also apparent that the KLE-templated BFO thin films calcined at 550 °C have lost most of their periodicity. This loss is particularly evident in the direction normal to the plane of the substrate (*z*-direction) because of the small number of repeat units and the high degree of contraction (note that very weak in-plane scattering maxima remained). The reason for the lack of periodicity is clearly due to the crystallization of the initially amorphous framework. This process is accompanied by a distinct restructuring of the distorted cubic pore network, as shown in Fig. 1. The appearance of new in-plane scattering maxima with a larger d-spacing (~50 nm) can also be attributed to the process of crystallizing the amorphous walls itself. These maxima represent the average particle-to-particle distance in the nanocrystalline BFO thin films.

Figure 3(a) shows SAXS data obtained on the same KLE-templated film used for GISAXS experiments. Although these Bragg–Brentano scans provide only information about the out-of-plane periodicity, they support the structure and morphology results. The fact that even a third order reflection can be observed for amorphous BFO, despite it being in thin film format, underlines the high degree of pore ordering. The shoulder peaks in the SAXS pattern of nanocrystalline BFO presumably correspond to the form factor of the elongated crystallites shown in Figs. 1(c) and 1(d).

Both Brunauer–Emmett–Teller (BET) surface area and pore volume were determined by krypton physisorption measurements at 87 K. Figure 3(b) shows typical adsorption–desorption isotherms for KLE-templated BFO thin films calcined at 550 °C for 20 min. The presence of a distinct condensation step at relative pressures of ~0.7 is characteristic of a material with

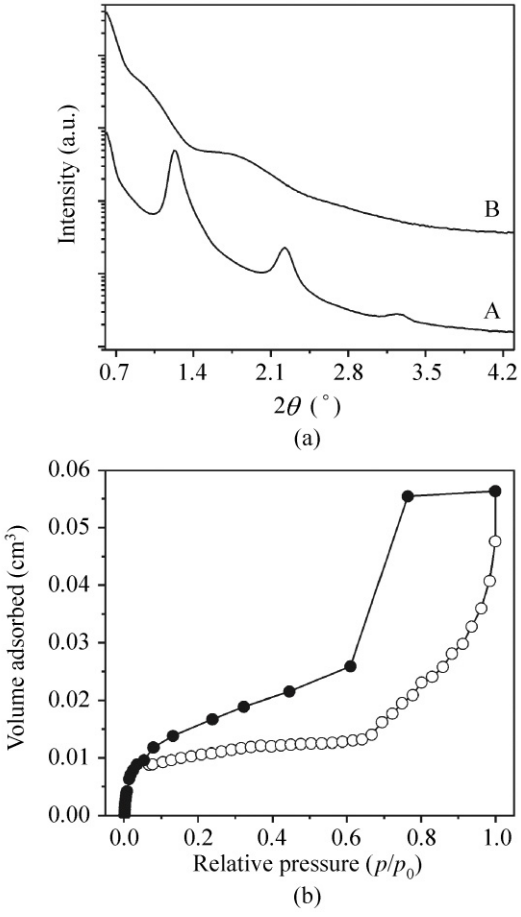

Figure 3 (a) SAXS patterns obtained on a KLE-templated BFO thin film with amorphous (A, 200 °C) and nanocrystalline framework (B, 550 °C). (b) Krypton adsorption–desorption isotherms for 80 nm thick KLE-templated BFO films with a total area of 45 cm^2. The type-Ⅳ shape is characteristic of a mesoporous material

open mesopore cavities that are interconnected through smaller necks. Using a saturation pressure of 13 torr and a cross-sectional area of 20.5 Å for krypton, a BET surface area of 130 m^2/cm^3 and a pore volume of 8.73×10^{-5} cm^3 (equivalent to 25% porosity) are obtained. We estimate the error margin as being ±5%.

To more fully characterize these materials, a series of wide-angle X-ray scattering (WAXS), Raman spectroscopy, and X-ray photoelectron spectroscopy (XPS) measurements were carried out. Figure 4(a) shows WAXS patterns obtained for KLE-templated BFO thin films calcined at 200 and 550 ˚C in air. It is evident from these data that samples aged at only 200 ˚C are fully amorphous. The crystallization occurs at about 550 ˚C, which is in agreement with observations for other BFO materials reported in the literature. The corresponding WAXS patterns reveal characteristic peaks for rhombohedral BFO, as corroborated with Joint Committee on Powder Diffraction Standards (JCPDS) reference card no. 86-1518. More importantly, neither pattern shows the presence of other phases—such as $Bi_2Fe_4O_9$ (#25-0090), α-Fe_2O_3 (#33-0664) or $Bi_2O_{2.33}$ (#27-0051)—which could potentially be formed during thermal treatment due to the presence of either iron- or bismuth-rich regions.

In recent years, it has been shown that the preparation of purely rhombohedral BFO by both solid-state synthesis and solution-processing routes is complicated due to the volatility of bismuth and bismuth oxide species. It is, however, known that impurities, such as the bismuth-poor $Bi_2Fe_4O_9$ phase, have a significant impact on material properties and performance. Since conventional WAXS techniques can be insensitive to very poorly crystalline materials and small amounts of second phases, Raman measurements were also carried out.

According to group theory, rhombohedral BFO has 18 optical phonon modes; $\Gamma = 4A_1 + 5A_2 + 9E$ [29]. The A_1(TO) and E(LO) modes are Raman and infrared active, while the A_2 modes are optically silent. A typical Raman spectrum of a KLE-templated BFO thin film calcined at 550 ˚C is shown in Fig. 5(a). The low-frequency A_1 modes appear at ~139, 167, and 222 cm^{-1} while the bands at ~77, 139, 266, 354, 374, and 477 cm^{-1} can be assigned to E modes [30]. The broad bands above 1000 cm^{-1} (indicated by 2E in Fig. 5(a)) have been

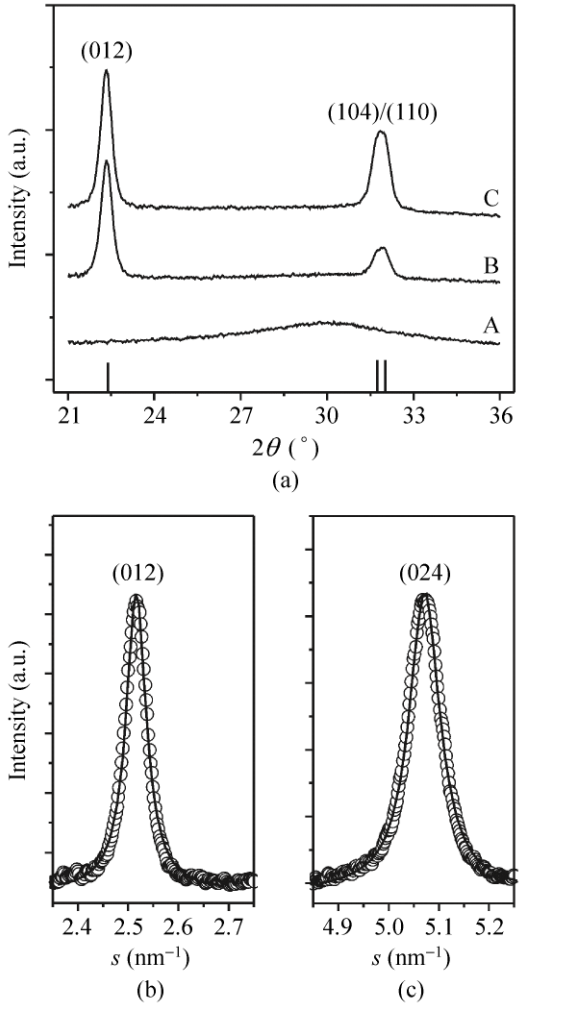

Figure 4 (a) WAXS patterns obtained on KLE-templated BFO thin films calcined at 200 ˚C for 2 h (A), 550 ˚C for 10 (B), and 20 min (C), respectively. The line pattern shows JCPDS reference card no. 86-1518. WAXS patterns showing both the (b) (012) and (c) (024) peaks of rhombohedral BFO; solid curves are Lorentzian fits to the experimental data. From these patterns, full width at half maximum (FWHM) intensities of ~0.05 and 0.075 nm^{-1} are obtained. The strong variation in the FWHM intensity indicates the presence of defects, such as lattice distortions and dislocations, and further implies that the actual crystallite domain size is different from that obtained by classical Scherrer analysis

shown to be related to two-phonon Raman scattering [31]. The fact that not all of the aforementioned Raman active phonon modes can be observed in Fig. 5(a) is due to superposition of the spectrum from the silicon substrate. Overall, both WAXS and Raman data collectively establish that the amount of second phases in the self-assembled BFO thin films is negligible (i.e., less than 2%).

The WAXS patterns in Fig. 4(a) further suggest that

the mesoporous BFO samples can be produced with a certain degree of crystallographic alignment, as evidenced by the relative intensity of the (012) peak compared to those at $2\theta = 31.9^\circ$ (note that the (110) peak is the most intense in polycrystalline BFO). In a recent publication, we have shown that materials with highly anisotropic unit cells, such as T-Nb_2O_5, L-Ta_2O_5 or α-MoO_3, exhibit oriented crystal growth on virtually any substrate and that the oriented nature of the nanocrystalline domains has a profound effect on material properties [26, 32]. For all of these systems, simulations suggested that the orientation is associated with minimizing interfacial energy by oriented crystal growth along certain crystallographic directions. We note, however, that the basis for the preferred crystallographic alignment in these materials is still not fully understood at this point. Nonetheless, BFO has an anisotropic unit cell and thus shows a certain degree of crystallographic alignment. This orientation, although relatively low compared to the materials mentioned above, however still corroborates our hypothesis.

The Warren–Averbach approach for analysis of WAXS patterns was applied to KLE-templated BFO thin films calcined at 550 ℃. This analysis provides a crystalline domain size of approximately 45 nm perpendicular to the substrate and an average maximum microstrain $\varepsilon = 0.008$. The Scherrer equation applied to the full width at half maximum (FWHM) intensity of the (012) and (024) peaks (see Figs. 4(b) and 4(c)), by contrast, indicates a much smaller domain size (< 20 nm). This result therefore suggests that a classical Scherrer analysis can be misleading for such materials. The average domain size in other crystallographic directions, however, could not be determined precisely on the basis of the WAXS data in Fig. 4. Both analyses further show that the domains formed at the onset of crystallization are instantly oriented with respect to the substrate and that their size cannot be tuned. This means that the peak widths do not change with increasing soak time. However, the growth of the peaks at $2\theta = 31.9^\circ$ indicates that extended aging reduces the degree of crystallographic alignment. This behavior emphasizes the fact that both the crystallite domain size and orientation are fundamentally coupled to the nanoscale network and cannot be altered without destroying that architecture.

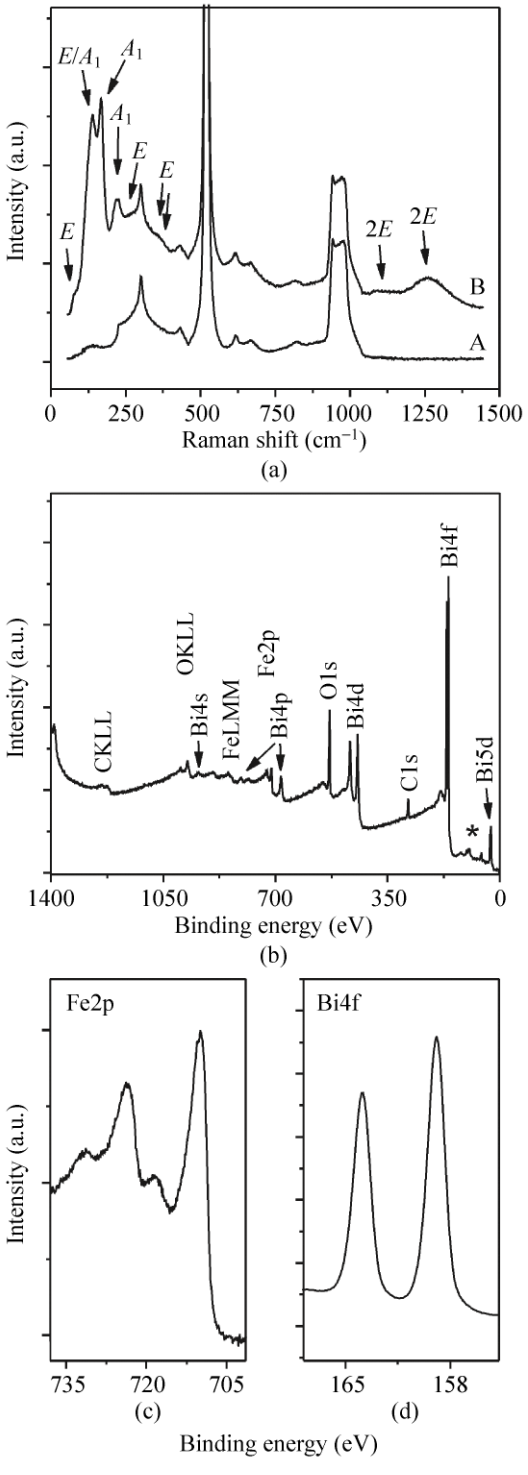

Figure 5 (a) Raman spectra obtained on a bare silicon substrate (A) and a KLE-templated BFO thin film calcined at 550 ℃ for 20 min (B). (b) Typical XPS survey spectrum. The asterisk indicates the Fe3s, Fe3p, and Bi5p core level regions. High resolution scans of the (c) Fe2p and (d) Bi4f levels

Figure 5(b) shows a typical XPS survey scan for KLE-templated BFO thin films calcined at 550 ℃.

Aside from a weak C 1s peak, which we associate with adventitious hydrocarbon, only bismuth, iron and oxygen core levels are observed. Figures 5(c) and 5(d) show high resolution XPS scans of the Fe 2p and Bi 4f regions. These levels consist of single doublets due to spin orbit splitting with binding energies of 723.47 eV ± 0.05 eV and 710.33 eV ± 0.05 eV for the $p_{1/2}$ and $p_{3/2}$ lines, respectively, and 163.83 eV ± 0.05 eV and 158.52 eV ± 0.05 eV for the $f_{5/2}$ and $f_{7/2}$ lines, respectively. We note that both the peak positions and separations (ΔBi_{4f} = 5.31 eV; ΔFe_{2p} = 13.14 eV) are consistent with reported measured values for rhombohedral BFO [33, 34]. Also, the presence of satellite peaks about 8 eV higher in binding energy than the main Fe 2p peaks indicates the presence of Fe^{3+} rather than Fe^{2+}. This result is not surprising, however, considering the high temperature calcination and the fact that Fe^{3+} is the stable oxidation state under the experimental conditions.

Lastly, TOF–SIMS measurements were carried out to determine whether both the iron and bismuth ions are homogeneously distributed throughout the films. TOF–SIMS depth profiles obtained on a KLE-templated BFO sample calcined at 550 °C are shown in Fig. S-3 (in the ESM). These spectra verify that the Fe^{3+} ions are in fact homogeneously distributed. The Bi^+ signal, by contrast, is of too low intensity to obtain any information that is qualitatively meaningful. Perhaps one reason for this is that a Bi^+ beam was used to generate secondary ions from the surface of the BFO films. Also, we find that the Fe^+ signal intensity increases near the sample/substrate interface. This result, however, does not imply that the Fe^{3+} ions are enriched at this interface but rather indicates a different chemical environment; the local environment is known to have a significant impact on the ionization probability. This conclusion is verified by the finding that both Na^+ and K^+ ions, which are always found as trace impurities even if the purest commercially available starting materials are used, reveal the same trend (see Fig. S-3 in the ESM). From the TOF–SIMS data, it is further evident that the organic template is completely removed throughout the films. Only minor amounts of hydrocarbons can be detected at the sample/air interface, which is in agreement with the XPS results in Fig. 5(b).

Apart from the typical scope of multiferroic BFO in the technology arena, it has been proposed that this material may be used as novel visible-light photocatalyst as well as in solid state devices that utilize heterojunction effects [11, 12]. For both of these applications, knowledge of the optical characteristics is crucial. However, there is conflicting information about these properties and band gap energy values varying from ~1 to 3 eV are reported in the Ref. [35, 36].

The following equation can be used to describe the dependence of absorption coefficient, α, on the difference between the photon energy of incident light, $h\nu$, and the band gap energy, E_g

$$\alpha \propto (h\nu - E_g)^n \quad (1)$$

In Eq. (1), n represents the type of optical transition. For n = 1/2, the transition is direct, while n = 2 indicates an indirect optical transition. Figure 6(a) shows plots for both types. However, the lack of the characteristic shape of the plot of $\alpha^{1/2}$ versus photon energy argues against an indirect optical transition in KLE-templated BFO thin films [35]. The band gap energy is estimated from the data for the direct transition as being 2.9 eV (equivalent to ~430 nm light). This value is in agreement with predictions and further suggests that nanoscale BFO might in fact be an effective visible-light photocatalyst [37].

To examine the photocatalytic properties of KLE-templated BFO, bleaching experiments were performed using rhodamine B (RhB) as a model pollutant. Figure 6(b) shows typical semilogarithmic plots which reveal that the degradation kinetics are pseudo-first-order. In addition, it can be clearly seen that the photobleaching of RhB in the absence of any catalyst is negligible. The degradation rate achieved using KLE-templated BFO thin films is about five times higher than that of samples prepared with no polymer template but under otherwise identical conditions. Since the density of the mesoporous BFO is significantly lower than the nontemplated films, this value underestimates the improvements produced by nanoscale porosity on a mass-normalized basis.

The nontemplated BFO thin films employed in this work are also crack-free on the micrometer level but possess a rather dense network structure (see Fig. S-1 in the ESM). Moreover, we find that these samples

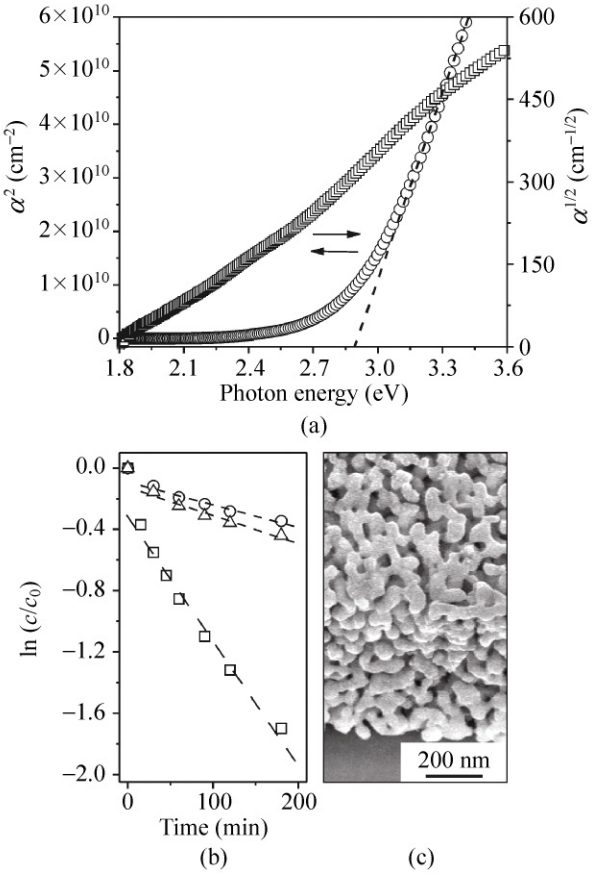

Figure 6 Optical and photocatalytic properties of KLE-templated BFO thin films calcined at 550 ˚C for 20 min. (a) Plots for both direct (○) and indirect (□) optical transitions. Extrapolation of the linear part of the curve to zero reveals a direct optical band gap at 2.9 eV. (b) Photobleaching of rhodamine B using KLE-templated (□, ~85% degradation after 180 min of irradiation), nontemplated thin films (△, ~35% degradation), and no photocatalyst (○). Dashed lines in (b) are linear fits to the experimental data. (c) Cross-sectional SEM image of a KLE-templated BFO thin film after photobleaching experiments showing that the film morphology is unaffected

cannot be produced in phase-pure form as opposed to KLE-templated BFO. WAXS data obtained on non-templated thin films show a small peak at $2\theta = 27.9^\circ$, which indicates the presence of trace amounts of the bismuth-rich sillenite phase (see Fig. S-4 in the ESM).

Apart from the control experiment with non-templated thin film catalysts we also examined the photodegradation of RhB using KLE-templated BFO calcined at 550 ˚C for 10 and 20 min with the goal of understanding whether the oriented nature of the nanocrystalline domains has an effect on photocatalytic activity. It turned out that the highest activity is achieved for samples that had been calcined for 20 min. Considering the fact that both materials have the same nanoscale architecture and very similar BET surface areas, this result indicates that the crystallographic alignment does not play an important role here. However, a different degree of crystallinity, which would certainly affect the activity, cannot be fully ruled out.

From Fig. 6(b) it is also apparent that the first data point was removed for linear regression analysis since this "outlier" did not fit the overall trend of the data. The reason for the faster degradation kinetics within the first 15 min of the initial cycle is not fully understood at this point. However, the data collected in the period after an initial exposure time of 15 min indicate a steady degradation of RhB over time. Moreover, we find that the KLE-templated BFO thin films are able to maintain stable performance over several cycles as there is no decline in photocatalytic activity. We associate this excellent stability with the fact that the mesoporous film morphology and the distorted perovskite structure both remain unaffected (see Figs. 6(c) and S-5 in the ESM).

Overall, the data in this section show that in contrast to nontemplated BFO thin films, the mesoporous samples are effective visible-light photocatalysts. We attribute this improvement to both the phase purity of the KLE-templated materials and the nanoscale porosity, the latter leading to more available active sites on the photocatalyst [38].

4. Conclusions

We have reported a facile block copolymer-directed synthesis of rhombohedral $BiFeO_3$ thin films with both a mesoporous morphology and nanocrystalline framework. The structure and morphology results clearly show that the KLE-templated samples are both homogeneous and crack-free at the micrometer level. Moreover, they also show that there is a distinct restructuring of the high quality cubic pore network of amorphous $BiFeO_3$ upon crystallization which leads to materials with a unique pore–solid architecture. More importantly, however, the data establish that the self-assembled thin films can be produced in phase-pure form.

The present work further demonstrates the benefits of combining a continuous mesoporosity with nanocrystalline thin films. Even though the BET surface area of our $BiFeO_3$ samples is lower compared to other KLE-templated materials, they exhibit a considerably better visible-light photocatalytic activity than that of films prepared with no polymer template. Overall, this research shows that nanoporous versions of single-phase $BiFeO_3$ are promising candidates for photocatalytic applications.

Future work will be dedicated to extending our synthesis method to solid solutions and more complex materials by replacing some of the bismuth and iron with other trivalent metal cations of similar radius in order to tune both the optical band gap energy and photocatalytic activity and to compete with well-known bismuth-based visible-light photocatalysts, such as $BiVO_4$ or Bi_2WO_6.

At this point we note again that apart from photocatalysis, such KLE-templated $BiFeO_3$ thin films could serve as exciting materials for host–guest applications. It is envisioned that the open porous network of these materials will facilitate the formation of novel exchange-coupled composites with intimate contact between the different components (e.g., electrically switchable magnets for spin valve/torque devices), which could pave the way for innovative device design. A study of the multiferroic properties is currently ongoing.

Acknowledgements

This work was supported by the Fonds der Chemischen Industrie through a Liebig fellowship (T. B.). Portions of this research were carried out at the German synchrotron radiation facility HASYLAB/DESY. The authors would also like to thank Jan Perlich, Bruno K. Meyer, Daniel Reppin, Bernd M. Smarsly, M. Rohnke, and Stephan V. Roth for their assistance in materials preparation and measurements.

Electronic Supplementary Material: Supplementary material (low- and high magnification electron microscope images of KLE-templated and nontemplated BFO; GISAXS patterns, Raman spectra, and TOF-SIMS depth profiles of KLE-templated BFO; WAXS data of nontemplated BFO) is available in the online version of this article at http://dx.doi.org/10.1007/s12274-011-0096-y.

References

[1] Ramesh, R.; Spaldin, N. A. Multiferroics: Progress and prospects in thin films. *Nat. Mater.* **2007**, *6*, 21–29.

[2] Stolichnov, I.; Riester, S. W. E.; Trodahl, H. J.; Setter, N.; Rushforth, A. W.; Edmonds, K. W.; Campion, R. P.; Foxon, C. T.; Gallagher, B. L.; Jungwirth, T. Non-volatile ferroelectric control of ferromagnetism in (Ga, Mn)As. *Nat. Mater.* **2008**, *7*, 464–467.

[3] Hill, N. A. Why are there so few magnetic ferroelectrics? *J. Phys. Chem. B* **2000**, *104*, 6694–6709.

[4] Eerenstein, W.; Mathur, N. D.; Scott, J. F. Multiferroic and magnetoelectric materials. *Nature* **2006**, *442*, 759–765.

[5] Cheong, S. W.; Mostovoy, M. Multiferroics: A magnetic twist for ferroelectricity. *Nat. Mater.* **2007**, *6*, 13–20.

[6] Catalan, G.; Scott, J. F. Physics and applications of bismuth ferrite. *Adv. Mater.* **2009**, *21*, 2463–2485.

[7] Chu, Y. H.; Martin, L. W.; Holcomb, M. B.; Gajek, M.; Han, S. J.; He, Q.; Balke, N.; Yang, C. H.; Lee, D.; Hu, W. et al. Electric-field control of local ferromagnetism using a magnetoelectric multiferroic. *Nat. Mater.* **2008**, *7*, 478–482.

[8] Wang, J.; Neaton, J. B.; Zheng, H.; Nagarajan, V.; Ogale, S. B.; Liu, B.; Viehland, D.; Vaithyanathan, V.; Schlom, D. G.; Waghmare, U. V. et al. Epitaxial $BiFeO_3$ multiferroic thin film heterostructures. *Science* **2003**, *299*, 1719–1722.

[9] Fiebig, M. Revival of the magnetoelectric effect. *J. Phys. D: Appl. Phys.* **2005**, *38*, R123–R152.

[10] Ederer, C.; Spaldin, N. A. Weak ferromagnetism and magnetoelectric coupling in bismuth ferrite. *Phys. Rev. B* **2005**, *71*, 060401.

[11] Gao, F.; Chen, X. Y.; Yin, K. B.; Dong, S.; Ren, Z. F.; Yuan, F.; Yu, T.; Zou, Z.; Liu, J. M. Visible-light photocatalytic properties of weak magnetic $BiFeO_3$ nanoparticles. *Adv. Mater.* **2007**, *19*, 2889–2892.

[12] Yang, H.; Luo, H. M.; Wang, H.; Usov, I. O.; Suvorova, N. A.; Jain, M.; Feldmann, D. M.; Dowden, P. C.; DePaula, R. F.; Jia, Q. X. Rectifying current–voltage characteristics of $BiFeO_3$/Nb-doped $SrTiO_3$ heterojunction. *Appl. Phys. Lett.* **2008**, *92*, 102113.

[13] Mills, A.; Davies, R. H.; Worsley, D. Water-purification by semiconductor photocatalysis. *Chem. Soc. Rev.* **1993**, *22*, 417–425.

[14] Hoffmann, M. R.; Martin, S. T.; Choi, W. Y.; Bahnemann, D. W. Environmental applications of semiconductor photocatalysis. *Chem. Rev.* **1995**, *95*, 69–96.

[15] Chatterjee, D.; Dasgupta, S. Visible light induced photocatalytic degradation of organic pollutants. *J. Photochem. Photobiol. C* **2005**, *6*, 186–205.

[16] Selbach, S. M.; Einarsrud, M. A.; Grande, T. On the thermodynamic stability of $BiFeO_3$. *Chem. Mater.* **2009**, *21*, 169–173.

[17] Mann, S.; Ozin, G. A. Synthesis of inorganic materials with complex form. *Nature* **1996**, *382*, 313–318.

[18] Yang, P. D.; Zhao, D. Y.; Margolese, D. I.; Chmelka, B. F.; Stucky, G. D. Block copolymer templating syntheses of mesoporous metal oxides with large ordering lengths and semicrystalline framework. *Chem. Mater.* **1999**, *11*, 2813–2826.

[19] Goltner, C. G.; Antonietti, M. Mesoporous materials by templating of liquid crystalline phases. *Adv. Mater.* **1997**, *9*, 431–436.

[20] Soler-Illia, G. J. D.; Sanchez, C.; Lebeau, B.; Patarin, J. Chemical strategies to design textured materials: From microporous and mesoporous oxides to nanonetworks and hierarchical structures. *Chem. Rev.* **2002**, *102*, 4093–4138.

[21] Brinker, C. J.; Lu, Y. F.; Sellinger, A.; Fan, H. Y. Evaporation-induced self-assembly: Nanostructures made easy. *Adv. Mater.* **1999**, *11*, 579–585.

[22] Brezesinski, T.; Wang, J.; Senter, R.; Brezesinski, K.; Dunn, B.; Tolbert, S. H. On the correlation between mechanical flexibility, nanoscale structure, and charge storage in periodic mesoporous CeO_2 thin films. *ACS Nano* **2010**, *4*, 967–977.

[23] Sel, O.; Sallard, S.; Brezesinski, T.; Rathousky, J.; Dunphy, D. R.; Collord, A.; Smarsly, B. M. Periodically ordered meso- and macroporous SiO_2 thin films and their induced electrochemical activity as a function of pore hierarchy. *Adv. Funct. Mater.* **2007**, *17*, 3241–3250.

[24] Brezesinski, K.; Ostermann, R.; Hartmann, P.; Perlich, J.; Brezesinski, T. Exceptional photocatalytic activity of ordered mesoporous β-Bi_2O_3 thin films and electrospun nanofiber mats. *Chem. Mater.* **2010**, *22*, 3079–3085.

[25] Richmann, E. K.; Kang, C. B.; Brezesinski, T.; Tolbert, S. H. Ordered mesoporous silicon through magnesium reduction of polymer templated silica thin films. *Nano Lett.* **2008**, *8*, 3075–3079.

[26] Brezesinski, K.; Wang, J.; Haetge, J.; Reitz, C.; Steinmueller, S. O.; Tolbert, S. H.; Smarsly, B. M.; Dunn, B.; Brezesinski, T. Pseudocapacitive contributions to charge storage in highly ordered mesoporous group V transition metal oxides with iso-oriented layered nanocrystalline domains. *J. Am. Chem. Soc.* **2010**, *132*, 6982–6990.

[27] Cseri, T.; Bekassy, S.; Kenessey, G.; Liptay, G.; Figueras, F. Characterization of metal nitrates and clay supported metal nitrates by thermal analysis. *Thermochim. Acta* **1996**, *288*, 137–154.

[28] Kodama, H. Synthesis of a new compound, $Bi_5O_7NO_3$, by thermal decomposition. *J. Solid State Chem.* **1994**, *112*, 27–30.

[29] Singh, M. K.; Jang, H. M.; Ryu, S.; Jo, M. H. Polarized Raman scattering of multiferroic $BiFeO_3$ epitaxial films with rhombohedral *R3c* symmetry. *Appl. Phys. Lett.* **2006**, *88*, 042907.

[30] Kothari, D.; Reddy, V. R.; Sathe, V. G.; Gupta, A.; Banerjee, A.; Awasthi, A. M. Raman scattering study of polycrystalline magnetoelectric $BiFeO_3$. *J. Magn. Magn. Mater.* **2008**, *320*, 548–552.

[31] Yang, Y.; Sun, J. Y.; Zhu, K.; Liu, Y. L.; Chen, J.; Xing, X. R. Raman study of $BiFeO_3$ with different excitation wavelengths. *Physica B* **2009**, *404*, 171–174.

[32] Brezesinski, T.; Groenewolt, M.; Pinna, N.; Amenitsch, H.; Antonietti, M.; Smarsly, B. M. Surfactant-mediated generation of iso-oriented dense and mesoporous crystalline metal-oxide layers. *Adv. Mater.* **2006**, *18*, 1827–1831.

[33] Moulder, J. F.; Stickle, W. F.; Sobol, P. E.; Bomben, K. D. *Handbook of Photoelectron Spectroscopy*; Perkin–Elmer Corp., Physical Electronics Division, Eden Prairie: Minnesota, USA, 1992.

[34] Jaiswal, A.; Das, R.; Vivekanand, K.; Abraham, P. M.; Adyanthaya, S.; Poddar, P. Effect of reduced particle size on the magnetic properties of chemically synthesized $BiFeO_3$ nanocrystals. *J. Phys. Chem. C* **2010**, *114*, 2108–2115.

[35] Gujar, T. P.; Shinde, V. R.; Lokhande, C. D. Nanocrystalline and highly resistive bismuth ferric oxide thin films by a simple chemical method. *Mater. Chem. Phys.* **2007**, *103*, 142–146.

[36] Li, J.; Collins, R. W.; Musfeldt, J. L.; Pan, X. Q.; Schubert, J.; Ramesh, R.; Schlom, D. G. Optical band gap of $BiFeO_3$ grown by molecular-beam epitaxy. *Appl. Phys. Lett.* **2008**, *92*, 142908.

[37] Clark, S. J.; Robertson, J. Band gap and Schottky barrier heights of multiferroic $BiFeO_3$. *Appl. Phys. Lett.* **2007**, *90*, 132903.

[38] Rolison, D. R. Catalytic nanoarchitectures—the importance of nothing and the unimportance of periodicity. *Science* **2003**, *299*, 1698–1701.